INL/JOU-25-85402-Revision-0

CFD Modeling of Turbulent Air Flow in Self-Heated Gyroid TPMS Structures: Thermal-Hydraulic Performance and Validation

August 2025

Silvino A Balderrama Prieto, Nicolas P. Martin, Brett A. Prussack, Austen David Fradeneck, Nicolas E Woolstenhulme, Mark H. Anderson

Changing the World's Energy Future

Idaho National Laboratory

INL is a U.S. Department of Energy National Laboratory operated by Battelle Energy Alliance, LLC

INL/JOU-25-85402-Revision-0

CFD Modeling of Turbulent Air Flow in Self-Heated Gyroid TPMS Structures: Thermal-Hydraulic Performance and Validation

Silvino A Balderrama Prieto, Nicolas P. Martin, Brett A. Prussack, Austen David Fradeneck, Nicolas E Woolstenhulme, Mark H. Anderson

August 2025

Idaho National Laboratory
Idaho Falls, Idaho 83415

http://www.inl.gov

Prepared for the
U.S. Department of Energy
Under DOE Idaho Operations Office
Contract DE-AC07-05ID14517

CFD Modeling of Turbulent Air Flow in Self-Heated Gyroid TPMS Structures: Thermal-Hydraulic Performance and Validation

Silvino A. Balderrama Prieto[a,*], Nicolas P. Martin[b], Brett A. Prussack[d], Austen D. Fradeneck[c], Nicolas E. Woolstenhulme[e], Mark H. Anderson[d]

[a]*Integrated Systems and Thermal Analysis, Energy and Environment Science & Technology, Idaho National Laboratory, 1955 N. Fremont Ave., Idaho Falls, Idaho, 83415, USA.*
[b]*Reactor Systems Design and Analysis Division, Nuclear Science & Technology, Idaho National Laboratory, 1955 N. Fremont Ave., Idaho Falls, Idaho, 83415, USA.*
[c]*Applied Engineering, Nuclear Science & Technology, Idaho National Laboratory, 1955 N. Fremont Ave., Idaho Falls, Idaho, 83415, USA.*
[d]*Thermal Hydraulics Laboratory, Department of Mechanical Engineering, University of Wisconsin-Madison, 1500 Engineering Drive, Madison, Wisconsin, 53706, USA.*
[e]*Nuclear Fuels and Materials, Nuclear Science & Technology, Idaho National Laboratory, 1955 N. Fremont Ave., Idaho Falls, Idaho, 83415, USA.*

Abstract

The application of mathematically derived geometries, such as triply periodic minimal surface (TPMS) lattices, has garnered significant interest across various fields, including the nuclear sector, due to their superior thermal-hydraulic characteristics for heat transfer compared to traditional plain or finned tubes. This study validates a computational fluid dynamics (CFD) model, evaluates different turbulence models and CFD model settings, and performs uncertainty quantification to provide a comprehensive analysis. Despite extensive research on CFD modeling of TPMS lattices, such as gyroid and diamond geometries, there is a notable lack of publicly available literature providing comprehensive details on numerical analysis aspects, including convergence and methodological best practices. This study embarks on a benchmark analysis of a gyroid geometry to evaluate its thermal-hydraulic performance under turbulent flow conditions and scrutinize various CFD model configurations. The main contributions of this work include validating the CFD model, assessing and comparing different turbulence models, and enhancing pressure drop and temperature prediction capabilities. The results aim to support the development of methodologies needed to benchmark and enhance numerical analysis techniques for TPMS lattices. This work seeks to complement the existing body of knowledge, support the development of TPMS reactor concepts, and improve best practices for CFD modeling of TPMS lattices, ultimately advancing methodologies to support future applications in this domain.

Keywords: TPMS lattice, Gyroid, Uncertainty analysis, Thermal-hydraulics, CFD

*Corresponding author
Email addresses: Silvino.BalderramaPrieto@inl.gov (Silvino A. Balderrama Prieto), Nicolas.Martin@inl.gov (Nicolas P. Martin), bprussack@wisc.edu (Brett A. Prussack), Austen.Fradeneck@inl.gov (Austen D. Fradeneck), Nicolas.Woolstenhulme@inl.gov (Nicolas E. Woolstenhulme), manderson@engr.wisc.edu (Mark H. Anderson)

August 25, 2025

1. Introduction

The use of triply periodic minimal surface (TPMS) geometries has gained significant interest across multiple disciplines, ranging from medical applications [1] to nuclear technology [2, 3]. TPMS geometries, derived from mathematical equations, result in unique structures that optimize material usage while maintaining strength and stability. Among the various TPMS geometries, the diamond and gyroid structures, as illustrated in Figure 1, are the most frequently referenced in the literature.

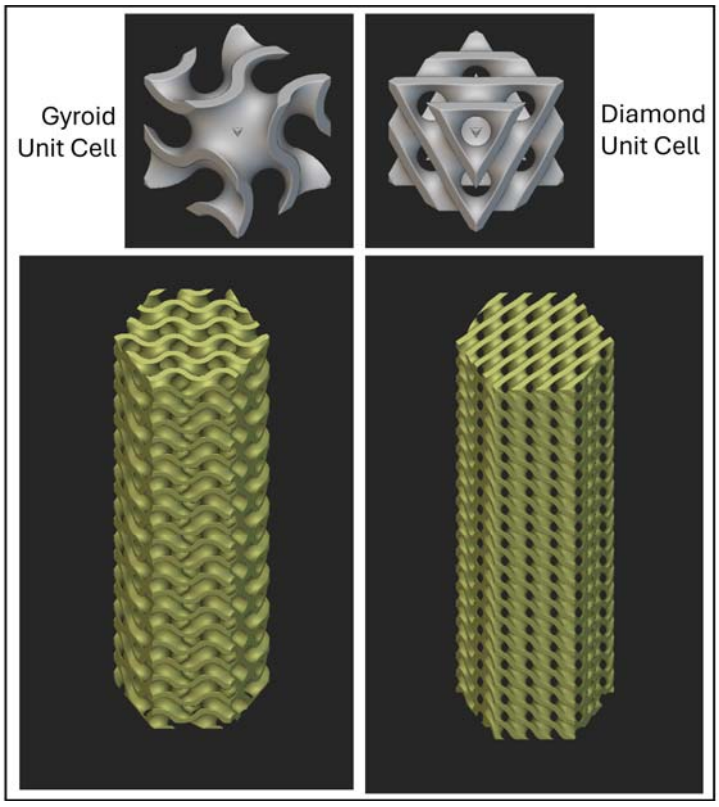

Figure 1: Comparison of TPMS geometries: gyroid (left) and diamond (right), featuring their respective unit cells (top) and hexagonal lattices (bottom).

The gyroid TPMS geometry has gained significant traction in the three-dimensional (3D) printing community, where it serves as an effective internal support structure for 3D parts [4]. In industrial applications, it has been successfully utilized in the development of compact heat sinks [5] and heat exchangers [6, 7, 8, 9] due to its high surface area per unit volume. Recently, its potential to enhance nuclear reactor designs has attracted significant attention. A study by Martin et al. [2] evaluated various TPMS geometries for their ability to meet the neutronic boundary conditions essential for sustaining a nuclear reactor core design. Additionally, a thorough thermal-hydraulic analysis is critical to determine their capability to improve thermal

performance and reduce costs in nuclear reactors.

In light of these developments, a Laboratory Directed Research and Development (LDRD) project at Idaho National Laboratory (INL) was initiated to explore the feasibility of advanced nuclear fuels and core designs leveraging TPMS geometries. The initiative is based on the recognized advantages of TPMS over conventional geometries in heat transfer applications [10, 9], which can provide substantial benefits to the nuclear industry. However, a comprehensive study on the application of TPMS structures in nuclear contexts requires experimental data to elucidate the underlying physics and to validate computational fluid dynamics (CFD) models. Validated CFD models can facilitate parametric studies and simulate complex physical phenomena that are difficult to measure experimentally. Despite the potential of CFD simulations, challenges such as numerical instability and non-convergence often hinder accurate modeling of thermal-hydraulics in TPMS under both isothermal and non-isothermal conditions.

While several journal articles have reported on the thermal-hydraulic performance of TPMS for heat sink and heat source applications, there remains a notable gap concerning pressure drop prediction, numerical stability, and convergence of CFD models. Existing studies have provided valuable insights into the thermal performance of TPMS geometries and their CFD modeling setups [9, 11, 3, 10, 6, 12]. However, a thorough investigation is still needed to assess thermal-hydraulic performance under turbulent flow conditions, evaluate various CFD model configurations, and enhance prediction capabilities for pressure drop and temperature.

This study aims to address these gaps by developing a deeper understanding of the CFD settings necessary for accurately predicting the thermal-hydraulics of TPMS geometries under turbulent flow conditions. The overall project aims to design and test TPMS nuclear fuel assemblies; however, the initial efforts presented in this study involve examining different turbulence settings and validating electrically heated TPMS using air as the heat transfer fluid (HTF). This study presents a novel electrical self-heating method to simulate the thermal behavior of nuclear fuel. These initial efforts will provide guidance for future TPMS modeling and experimentation with other fluids relevant to nuclear systems involving self-heated TPMS lattices. Additionally, a comprehensive analysis of numerical uncertainty and convergence will be conducted, providing valuable insights to inform future modeling efforts of these intricate geometries. This is an initial effort, and it is hoped that researchers in the future will take this information and improve upon it for better thermal-hydraulic predictions of the physics within TPMS using CFD tools.

2. TPMS Geometry

TPMS are mathematically defined geometries generated using trigonometric level-set approximation equations. These equations describe surfaces where specific trigonometric functions result in a constant value, often denoted by the variable "C". Essentially, the generated surface is implicitly defined as the zero-level set of these equations, meaning the surface represents points in space where the equation evaluates to this constant value. TPMS geometries are notable for their complex structures and have applications in various fields due to their unique properties. In this study, the gyroid, a widely used TPMS geometry, was generated using the following level-set equation:

$$\sin(x)\cos(x) + \sin(y)\cos(y) + \sin(z)\cos(z) = C \tag{1}$$

Equation 1 defines a complex, continuous surface that separates two distinct regions of space without any self-intersections. The gyroid is unique because it lacks planar symmetry and is

non-self-intersecting, making it useful in various applications such as heat exchangers, filters, and photonic crystals due to its high surface area and structural integrity.

The initial solution to the gyroid level-set equation produces a surface with zero thickness, making it an idealized mathematical surface. To use this surface in practical applications, it needs to be converted into a solid geometry. There are two common approaches for this:

1. **Single-Sided Filling**: One side of the surface can be filled with solid material, while the other side remains fluid or empty. This approach treats the TPMS as a boundary that separates solid and fluid regions.
2. **Dual-Sided Thickening**: This method involves increasing the surface thickness equally in both directions, creating a solid volume around the original surface. This allows the TPMS to have a defined thickness, which is essential for structural integrity and manufacturability in applications such as additive manufacturing.

In this study, the second approach, thickening the gyroid surface in both directions, was implemented. The commercial software nTop was used to generate the gyroid TPMS with the desired thickness. This way, the gyroid geometry serves as a boundary that defines separate solid and fluid regions within the computational domain.

The Reynolds number (Re) is an important non-dimensional parameter that describes the flow characteristics within and around TPMS geometries such as the gyroid. The Reynolds number can be expressed in terms of mass flow rate ($\dot{m}$), and its mathematical expression is as follows:

$$Re = \frac{\dot{m} D_h}{\mu A_{cross}} \tag{2}$$

where $\dot{m}$ is the mass flow rate (kg/s), D_h is the hydraulic diameter of the gyroid lattice (m), A_{cross} is the cross-sectional area (m^2), and μ is the dynamic viscosity of the fluid (Pa-s). For non-circular cross-sections, such as TPMS geometries, the hydraulic diameter can be computed as:

$$D_h = \frac{4V_f}{A_s} \tag{3}$$

From the above expression, V_f represents the volume of the fluid region, and A_s denotes the wetted surface area. Utilizing the mass flow rate simplifies the analysis, especially when the flow rate is easier to measure or control compared to flow velocity. The hydraulic diameter, which depends on the characteristic channel size within the gyroid structure, is crucial for determining the Reynolds number and assessing whether the flow is laminar or turbulent. It is essential to note that the hydraulic diameter of the gyroid TPMS is not constant along the unit cell size. Instead, it fluctuates periodically, similar to the flow area (refer to Figure 2) [8].

As a result of the flow area fluctuation, it was deemed necessary to calculate the hydraulic diameter as a function of V_f and A_s. By incorporating the volume of the fluid region and the wetted surface area into the calculation, we can better predict the flow characteristics and ensure precise determination of the Reynolds number.

3. Experimental Setup

INL and the University of Wisconsin (UW) - Madison collaborated to build an experimental facility designed to test self-heating TPMS geometries using air as the HTF. The primary purpose

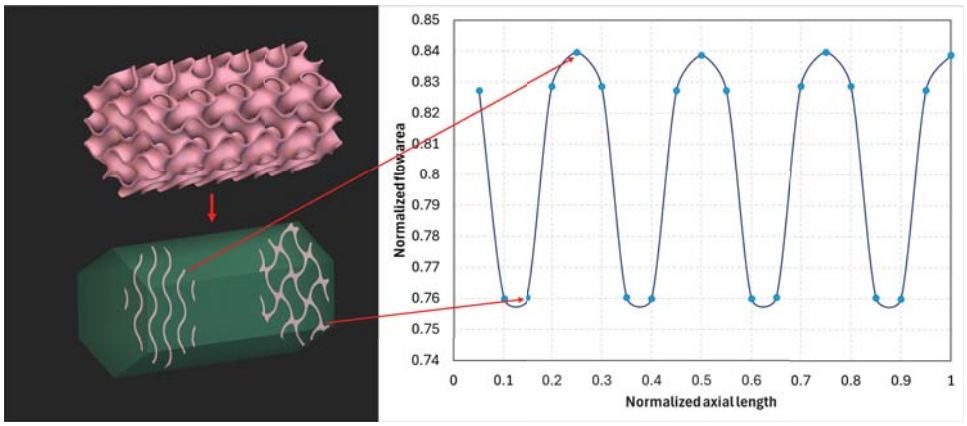

Figure 2: Variation of flow area along a gyroid TPMS geometry. The flow cross-sectional area is normalized by the total frontal flow area and the axial length is normalized by the unit cell size.

of this facility is to generate experimental data on TPMS geometries that could be applied in nuclear contexts. Before conducting experiments with nuclear fuels, UW constructed an out-of-pile experimental facility to test self-heating TPMS geometries, simulating the fission heating that occurs in nuclear fuels. The initial phase of the research involves experiments using air to establish a baseline before transitioning to other fluids relevant to nuclear systems.

3.1. Lattice Fabrication and Preparation

The test articles were meticulously designed utilizing the gyroid TPMS equation to generate hexagonal gyroid lattices, as shown on the left-hand side of Figure 1. These lattices were saved in an STL file format, which was subsequently employed to 3D print the test articles using electrically conductive polylactic acid (PLA) filament, Proto-pasta [13]. The 3D printing process was carried out with a layer height of 0.15 mm on an Ultimaker S3 printer.

To integrate temperature measurement capabilities, the printing process was paused at the mid-plane, where channels were designed to allow thermocouples (TCs) to be press-fitted into place and secured with a high-temperature adhesive. Six embedded TCs, manufactured in-house from perfluoroalkoxy insulated K-type 30-gauge wire (Omega TT-K-30-SLE), measured the solid wall temperature and the fluid temperature at three locations along the centerline of the lattice: the first open channel at the inlet, at the middle 50 mm downstream from the inlet, and at the exit in the last centerline open channel, as shown in Figure 3. These measurements were used to estimate the local heat transfer coefficient. Once the TCs were embedded, the print was then resumed and completed. finally, the test section was wrapped with fiberglass insulation to minimize heat loss to the environment.

A comprehensive summary of the gyroid TPMS geometry properties is provided in Table 1. This detailed information is essential for understanding the geometric parameters that influence the fluid dynamic performance of the test articles. Furthermore, the use of electrically conductive PLA filament enabled the application of direct current (DC) voltage for volumetric heating, simulating the conditions found in nuclear fuel applications. This innovative approach allows for precise control of the thermal environment within the test section, providing valuable insights into the heat transfer capabilities of TPMS geometries.

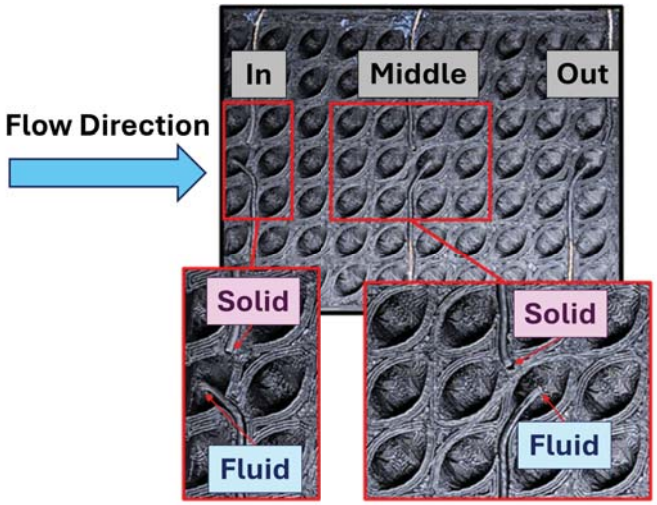

Figure 3: Embedded K-type TCs within the TPMS lattice for temperature measurement in both solid and fluid regions at the inlet, middle, and outlet.

Table 1: Summary of TPMS geometry characteristics.

Description	Value
TPMS geometry	Gyroid
Axial length	100.0 mm
Porosity	0.3693
Solid volume	171,272 mm^3
Total volume	271,558 mm^3
Hexagonal area	2,716 mm^2

3.2. Experimental Facility

The facility consists of a compressed air line that forces the HTF, at approximately room temperature, through the 3D-printed gyroid lattice test article at mass flow rates ranging from 5 to 25 g/s. A Swagelok integral bonnet needle valve (Cv=1.8) was installed to control the flow rate, which was measured with a Flow-Dyne venturi flow meter. The pressure drop within the venturi was measured between the throat and expansion section using a Rosemount differential pressure transducer (Rosemount 3051) with an accuracy of ±0.025% [14]. The absolute pressure of the air, necessary for determining fluid properties, was measured using a Rosemount 3051T pressure transmitter (span accuracy ±0.04%) [15], located immediately downstream of the venturi flow meter. The experimental apparatus used to validate the CFD simulations is shown in Figure 4.

The pipe size gradually increased to a 2.5-inch NPS schedule 10 stainless-steel pipe, where the fluid's centerline temperature was measured using a K-type Omega TC. The differential pressure across the test section was measured using a Siemens Sitrans-P pressure transducer, with taps located 30 mm from the inlet and outlet. The downstream temperature of the fluid was then measured. Finally, the pipe was reduced to its original diameter, and the air was exhausted into the atmosphere. All data were monitored and collected using a LabVIEW program in conjunc-

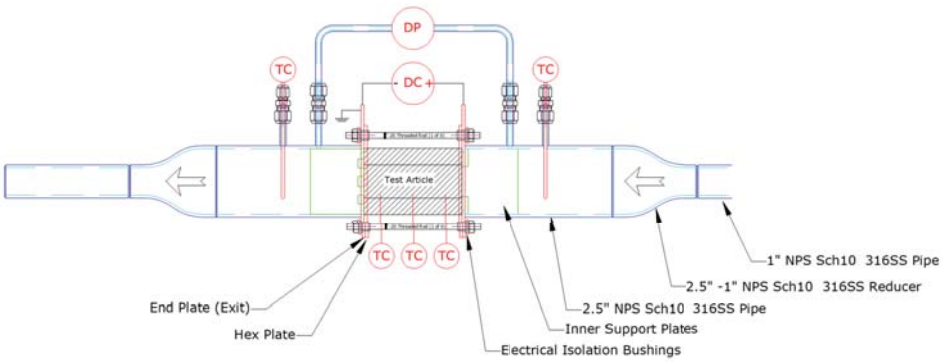

Figure 4: Schematic of the UW-Madison test bed for electrically-heated TPMS, illustrating the instrumentation layout.

tion with a National Instruments data acquisition system.

Threaded rods were used to clamp the test article between two laser-cut stainless-steel electrode plates, aligning with the inlet and outlet faces of the test article. A silver-filled electrically conductive epoxy (AI Technology EG8050) was applied to enhance electrical contact between the conductive PLA test article and the electrode plates. The electrode plates were then connected to a DLM-300-13E DC power supply, with the positive terminal connected to the right plate, as indicated in red in Figure 5, and the negative terminal connected to the left plate. This configuration facilitated the passage of current through the test article. As the power supply was turned on and adjusted according to experimental needs, the conductive PLA heated up due to the current passing through it, resulting in volumetric heat generation within the solid material. To ensure that the current was directed solely through the test article, the remainder of the test section and instruments were electrically insulated, preventing any unintended current draw from the power supply.

Data were collected during the steady-state operation of the test article. First, the desired flow rate was established through the test section. Next, the desired power was applied, and the system was allowed to reach steady-state conditions. Once steady-state was achieved, data were recorded for 20 seconds at a rate of 2 samples per second. The recorded data were then averaged to obtain a single data point at the desired flow rate and load.

3.3. Experimental Uncertainty

The method used to quantify the uncertainty of a measurement resulting from multiple factors is the root-sum-of-squares (RSS) method. This method calculates the combined uncertainty (u_c), which is the square root of the sum of the squares of the individual standard uncertainties (u_i) from each measurement, as shown in Equation 4.

$$u_c = \sqrt{\sum_{i=1}^{n} [c_i u_i]^2} \tag{4}$$

In the above equation, c denotes the sensitivity coefficient. In this study, we also utilize the expanded uncertainty (u_e), which is the combined uncertainty multiplied by a coverage factor

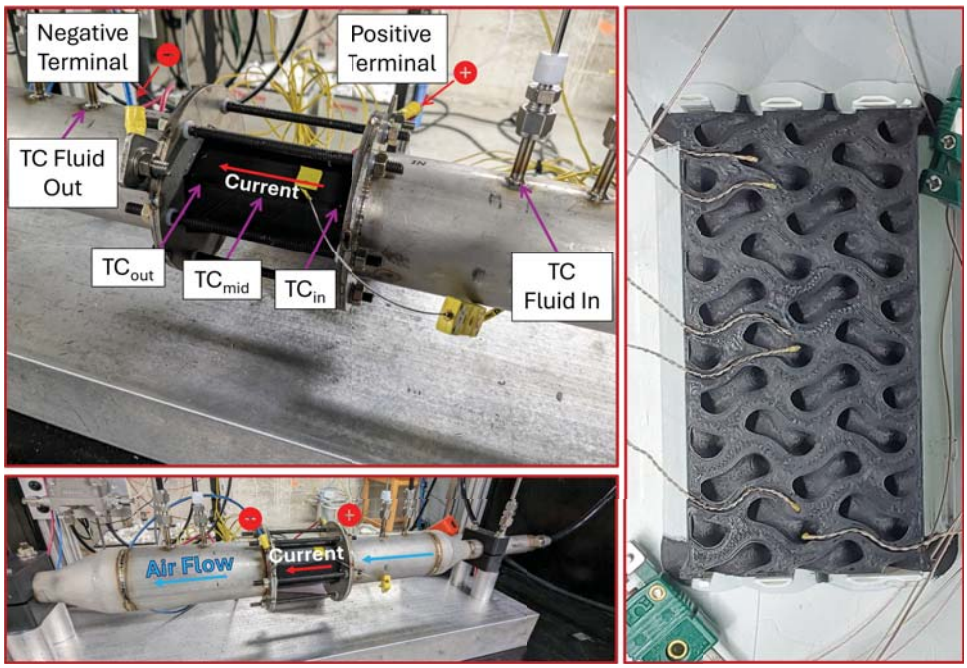

Figure 5: Top left: Overview of the UW experimental setup, showcasing the arrangement of equipment and sensors. Right: Close-up of a thermocouple strategically embedded within the TPMS lattice structure. Bottom left: Detailed view of the experimental setup, highlighting the air flow direction (blue) and electrical current direction (red).

(λ), to accommodate the desired confidence level in the measurements, refer to Equation 5. A coverage factor of 2 is applied to compute the expanded uncertainty with a 95% confidence level.

$$u_e = \lambda \cdot u_c \tag{5}$$

The accuracy of the k-type TCs is 0.75% or 2.2°C, whichever value is larger [16]. Given that the experiments were conducted at room temperature, the sensors should have a standard error limit of ±2.2°C. The uncertainty of the temperature measurements was determined by assuming a rectangular distribution for the standard uncertainties and a sensitivity coefficient of 1. A repeatability study encompassing four measurements was carried out. The results of this uncertainty quantification are summarized in Table 2.

Table 2: Calculated combined and expanded uncertainty for temperature measurements.

Uncertainty component	**Distribution**	**Uncertainty**	**Contribution percentage**
Accuracy (u_a)	Rectangular	2.2	64.85%
Repeatability (u_r)	Rectangular	0.83	35.15%
Combined uncertainty (u_c)		2.4°C	-
Expanded uncertainty (λ=2) 95% confidence		**4.7°C**	-

The uncertainty associated with the pressure measurements was calculated using a similar

approach to the one outlined for the temperature measurements. The Rosemount differential pressure has an accuracy of ±0.025%, whereas the absolute pressure transducer has an accuracy of ±0.04%. Based on the obtained measurements and the repeatability study, the differential pressure measurements have an uncertainty of 90.91 Pa with a 95% confidence level. The absolute pressure measurements, on the other hand, have an uncertainty of 9353 Pa with a 95% confidence level. A summary of the values used to compute the expanded uncertainty is presented in Tables 3 and 4.

Table 3: Calculated combined and expanded uncertainty for absolute pressure measurements.

Uncertainty component	**Distribution**	**Uncertainty**	**Contribution percentage**
Accuracy (u_a)	Rectangular	252.3	0.15%
Repeatability (u_r)	Rectangular	4670	99.85%
Combined uncertainty (u_c)		4677 Pa	-
Expanded uncertainty (λ=2) 95% confidence		**9353 Pa**	-

Table 4: Calculated combined and expanded uncertainty for differential pressure measurements.

Uncertainty component	**Distribution**	**Uncertainty**	**Contribution percentage**
Accuracy (u_a)	Rectangular	0.1228	0.01%
Repeatability (u_r)	Rectangular	45.46	99.99%
Combined uncertainty (u_c)		45.46 Pa	-
Expanded uncertainty (λ=2) 95% confidence		**90.91 Pa**	-

The mass flow rate is obtained using the fluid density, pressure difference from upstream to the throat of the venturi meter (Δp_v), the expansion factor (ε), the venturi's throat diameter (d_t) and downstream diameter (d_d), the discharge coefficient (C_d), and the venturi meter cross-sectional area at the throat (A_t). The mathematical function to calculate for the mass flow rate is shown in Equation 6 [17].

$$\dot{m} = C_d A_t \varepsilon \sqrt{\frac{2\rho \Delta p_v}{1 - (d_t/d_d)^4}} \tag{6}$$

The mass flow rate's uncertainty can be determined using uncertainty propagation, where the uncertainty in the mass flow rate is calculated based on the uncertainties in the pressure drop across the venturi and the air density. Equation 7 presents the general mathematical expression for calculating uncertainty propagation [18].

$$u_f = \sqrt{\left(\frac{\partial f}{\partial x_1} u(x_1)\right)^2 + \left(\frac{\partial f}{\partial x_2} u(x_2)\right)^2 + \cdots + \left(\frac{\partial f}{\partial x_n} u(x_n)\right)^2} \tag{7}$$

The partial derivatives can be determined by employing Equations 8 and 9. The uncertainty from diameters, and discharge coefficient can be neglected due to its negligible impact on the mass flow rate uncertainty.

$$\frac{\partial \dot{m}}{\partial \Delta p_v} = C_d A_t \varepsilon \frac{\rho}{\sqrt{\Delta p_v}} \sqrt{\frac{2}{1 - (d_t/d_d)^4}} \tag{8}$$

$$\frac{\partial \dot{m}}{\partial \rho} = C_d A_t \varepsilon \sqrt{\frac{2\Delta p_v}{\rho}} \sqrt{\frac{1}{1-(d_t/d_d)^4}} \tag{9}$$

By replacing Equations 8 and 9 into Equation 7, it yields the following function:

$$u_{\dot{m}} = \sqrt{\left(C_d A_t \varepsilon \frac{\rho}{\sqrt{\Delta p_v}} \sqrt{\frac{2}{1-(d_t/d_d)^4}} u_{\Delta p_v}\right)^2 + \left(C_d A_t \varepsilon \sqrt{\frac{2\Delta p_v}{\rho}} \sqrt{\frac{1}{1-(d_t/d_d)^4}} u_\rho\right)^2} \tag{10}$$

The combined and expanded uncertainty for the mass flow rate is summarized in Table 5.

Table 5: Calculated uncertainty of mass flow rate measurements obtained from the venturi flow meter.

Description	Distribution	Value
Uncertainty contribution from air density (ρ) [kg/m^3]	Rectangular	$2.77 \cdot 10^{-4}$
Uncertainty contribution from venturi's pressure drop (Δp_v) [Pa]	Rectangular	62.0
Venturi's throat diameter (d_t) [in./m.]		0.215/0.006
Downstream diameter (d_d) [in./m.]		0.870/0.022
Discharge coefficient (C_d) [-]		0.995
Expansion factor [K^{-1}]		0.004
Uncertainty (u_m) [kg/s]		$2.47 \cdot 10^{-4}$

4. Numerical Modeling of TPMS

CFD modeling of a TPMS is a complex process, particularly when trying to achieve numerical convergence. This section discusses the governing equations employed in the CFD software to solve the case scenario under consideration, evaluates different turbulence models to improve the model's prediction capabilities, and other settings that support numerical stability and convergence. To evaluate the prediction performance of the CFD models, a validation study is conducted using experimental data as a basis to determine the model's capability to accurately recreate real-world phenomena.

The validation approach involves recreating the electrically heated TPMS experimental data collected by UW. This validation study assesses the assumptions, physics models, boundary conditions, and the numerical uncertainty introduced by spatial discretization. Special attention is given to the evaluation of spatial discretization, aiming to identify the ideal mesh size for accurate modeling of the phenomena occurring within the TPMS. The goal is to use a mesh large enough to capture significant phenomena while being small enough to capture relevant details without creating computationally expensive models.

4.1. Governing Equations

The computational domain of the TPMS geometry was created using the STL file generated for the 3D-printed lattices. This file was imported into the commercial software STAR-CCM+ 2406 (19.04.009-R8 double precision) to generate the solid and fluid regions. Once the domain was established, it was crucial to ensure accurate simulation of the physical processes within these regions. To achieve this, the fundamental conservation equations of mass, momentum, and

energy, which govern fluid flow and heat transfer, were applied. These equations are essential for capturing the dynamics within the TPMS structure and were implemented to model the complex interactions between the solid and fluid phases in the computational domain.

The continuity equation, a fundamental principle in fluid dynamics simulations, ensures mass conservation and is presented in Equation 11.

$$\nabla \cdot (\rho \vec{v}) = 0 \tag{11}$$

In Equation 11, ρ represents the fluid density, and $\vec{v}$ denotes the fluid velocity vector. This equation states that the rate of mass entering a control volume is equal to the rate of mass leaving it, ensuring that mass is neither created nor destroyed within the flow field.

The energy equation, which accounts for thermal effects within the fluid, is expressed mathematically as follows:

$$\nabla \cdot (\rho E \vec{v}) = -\nabla \cdot (k \nabla T) + \nabla \cdot (\mu \vec{v} \cdot \nabla \vec{v}) + \rho \vec{v} \cdot \vec{g} \tag{12}$$

In this equation, (E) is the total energy per unit volume, which includes internal energy and kinetic energy of the fluid, (T) is the fluid temperature, and (k) is the thermal conductivity. The left-hand side represents the convective transport of energy. The right-hand side includes the heat conduction term, the viscous dissipation term, and the work done by the gravitational force. This equation is essential for predicting temperature distributions and thermal effects within the fluid.

The momentum equation, another critical component in fluid dynamics, governs the conservation of momentum and is given by:

$$\nabla \cdot (\rho \vec{v} \vec{v}) = -\nabla p + \nabla \cdot (\mu \nabla \vec{v}) + \rho \vec{g} \tag{13}$$

where p is the pressure, and $\vec{g}$ represents the gravitational acceleration vector. The left-hand side of the equation represents the convective transport of momentum. The right-hand side encompasses the pressure gradient force, the viscous forces (or shear stress), and the body force due to gravity. This equation describes how the momentum of the fluid is influenced by these forces.

The modeling of turbulence can be addressed using several turbulence models. The main turbulence models employed in this analysis are the Reynolds-averaged Navier-Stokes (RANS) realizable k-epsilon (k-ε) two-layer model and the k-omega (k-ω) Menter Shear Stress Transport (SST) model, along with Lag Elliptic Blending (LEB) k-ε model.

The realizable k-ε model is beneficial for its robustness in predicting the mean flow characteristics for a wide range of turbulent flows, including those with complex geometry and flow separation [19].

The realizable k-ε model is governed by the following equations:

$$\frac{\partial(\rho k)}{\partial t} + \frac{\partial(\rho k u_j)}{\partial x_j} = \frac{\partial}{\partial x_j}\left(\left(\mu + \frac{\mu_t}{\sigma_k}\right)\frac{\partial k}{\partial x_j}\right) + G_k + G_b - Y_M + S_k - \rho\varepsilon \tag{14}$$

$$\frac{\partial(\rho \varepsilon)}{\partial t} + \frac{\partial(\rho \varepsilon u_j)}{\partial x_j} = \frac{\partial}{\partial x_j}\left(\left(\mu + \frac{\mu_t}{\sigma_\varepsilon}\right)\frac{\partial \varepsilon}{\partial x_j}\right) + \rho C_1 S_\varepsilon - \rho C_2 \frac{\varepsilon^2}{k + \sqrt{\nu\varepsilon}} + C_{1\varepsilon}\frac{\varepsilon}{k} C_{3\varepsilon} G_b + S_\varepsilon \tag{15}$$

where

$$C_1 = max\left[0.43, \frac{\eta}{\eta + 5}\right], \quad \eta = S\frac{k}{\varepsilon}, \quad S = \sqrt{2 S_{ij} S_{ij}} \tag{16}$$

From above, μ_t is the turbulent eddy viscosity, G_k denotes the production of turbulence kinetic energy from mean velocity gradients, while G_b is the production of turbulence kinetic energy due to buoyancy. The term Y_M accounts for the impact of fluctuating dilatation in compressible turbulence on the overall dissipation rate. C_2 and $C_{1\varepsilon}$ are constants, and σ_k and σ_ε are the turbulent Prandtl numbers for k and ε, respectively. S_k and S_ε are user-defined source terms.

The k-ω SST model, on the other hand, combines the advantages of the k-omega model in the near-wall region with the k-ε model in the far-field. This hybrid approach allows for better prediction of boundary layer properties and flow separation, making it suitable for handling adverse pressure gradients and transition flows [20]. The k-omega SST model is governed by the following equations:

$$\frac{\partial(\rho k)}{\partial t} + \frac{\partial(\rho k u_j)}{\partial x_j} = \frac{\partial}{\partial x_j}\left((\mu + \mu_t \sigma_k)\frac{\partial k}{\partial x_j}\right) + G_k + G_b + G_{nl} - \beta^* \rho f_{\beta^*}(\omega k - \omega_o k_o) + S_k \tag{17}$$

$$\frac{\partial(\rho \omega)}{\partial t} + \frac{\partial(\rho \omega u_j)}{\partial x_j} = \frac{\partial}{\partial x_j}\left((\mu + \mu_t \sigma_\omega)\frac{\partial \omega}{\partial x_j}\right) + G_\omega + D_\omega - \beta \rho f_\beta(\omega^2 - \omega_o^2) + S_\omega \tag{18}$$

where σ_ω is the turbulent Prandtl number for the specific dissipation rate ω, f_{β^*} is the free-shear modification factor, f_β is the vortex-stretching modification factor, S_ω is a user-specified source term, k_o and ω_o are the ambient turbulence values that counteract turbulence decay, G_ω is the specific dissipation production, D_ω is the cross-diffusion term, G_{nl} is the non-linear production term, and β and β^* are model coefficients.

The LEB model combines the Standard Elliptic Blending model, which solves transport equations for turbulent kinetic energy (k), turbulent dissipation rate (ε), normalized wall-normal stress component, and the elliptic blending factor to determine turbulent eddy viscosity, with the stress-strain lag concept introduced by Revell et al. [21].

In flow regions where non-equilibrium effects lead to a misalignment between the principal components of the stress and strain-rate tensors, linear eddy viscosity models tend to overestimate the turbulent kinetic energy. The LEB model incorporates the angle between these components to mitigate this overestimation. For further information, it is recommended to consult the STAR-CCM+ user guide [22].

The application of these continuity, momentum, energy, and turbulence equations in STAR-CCM+ is essential for accurately simulating fluid flow and heat transfer in complex geometries such as TPMS structures. These equations provide the foundational principles that ensure the reliability and precision of the simulations, thereby enabling a thorough evaluation of hydraulic and thermal performance metrics.

4.2. Spatial Discretization

The spatial discretization of the fluid and solid regions of the TPMS was created using a polyhedral mesh with a base size of 0.35 mm. To better capture the curvature of the gyroid TPMS, the minimum surface size was adjusted from its default value of 10% to 5% relative to the base size. For modeling the boundary layer, a prism layer mesh model was adopted primarily to capture the fluid behavior near the TPMS walls. Achieving a conformal mesh between the solid and fluid regions required special treatment. A surface control option was implemented to customize the mesh of the solid near the fluid region, ensuring improved discretization between these two areas. Figure 6 displays the computational domain along with its dimensions.

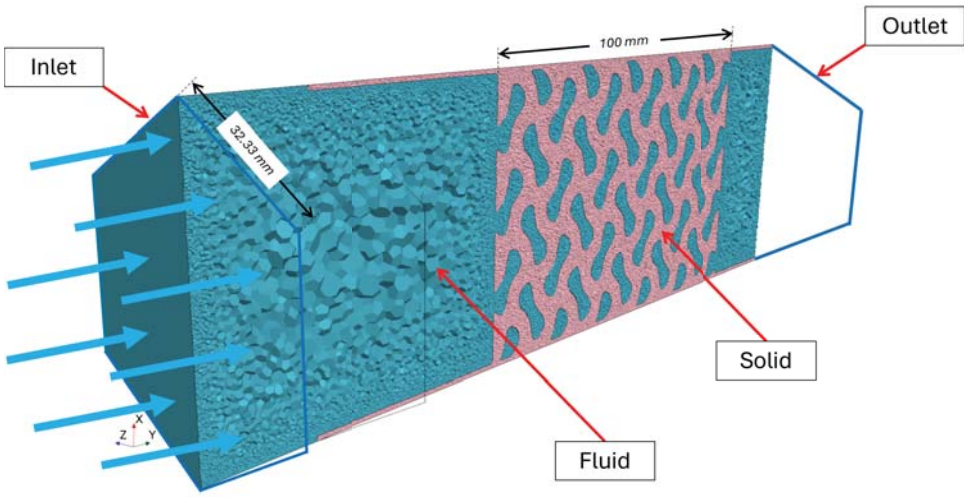

Figure 6: Cross-sectional view of a gyroid TPMS computational domain, showcasing a half-section. The solid region, comprising the gyroid structure, is represented in pink, while the fluid region is depicted in blue.

The number of prism layers for the solid region was reduced from five to one to streamline the mesh while maintaining accuracy. In contrast, the fluid region retained its imposed five prism layers, which proved effective in capturing the boundary layer across a wide range of flow rates. The total prism layer thickness was customized to an absolute value of $3.75{\cdot}10^{-5}$ m. Figure 7 showcases the discretization of the solid and fluid regions, highlighting the efforts made towards accurately discretizing the regions near the TPMS wall.

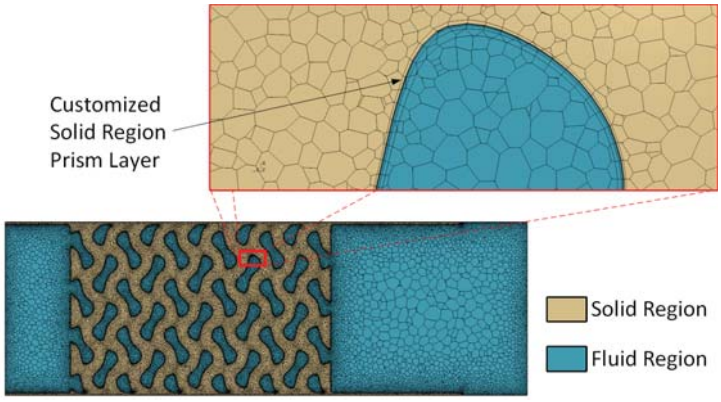

Figure 7: Spatial discretization of the solid and fluid regions of a gyroid TPMS using STAR-CCM+ meshing software.

Meshing these types of geometries required further optimization, particularly when using the k-ω (Menter) SST turbulence model due to its sensitivity to cell quality when calculating the cross-diffusion term [23]. To address this, the optimization cycle of the core mesh was

activated and customized to perform five cycles with a quality threshold of 0.5, resulting in a high-quality mesh. It is important to note that while five optimization cycles were adopted for this study, other users may choose to perform more or fewer cycles based on their specific case study. Additionally, post-optimization options for the boundary vertices and cell topology were activated to further enhance mesh quality. A summary of the mesh settings adopted in this study is provided in Table 6.

Table 6: Overview of mesh settings used for the spatial discretization of a Gyroid TPMS geometry.

Surface Remesher (Method: enhanced quality triangle) Polyhedral Mesher Prism Layer Mesher (Distribution mode: wall thickness)	Base size: 0.375 mm Minimum surface size: 5% Surface growth rate: Slow Number of prism layers: 5 Prism layer total thickness: 0.125 mm
Surface Controls	Customize number of prism layers: 1 Customize total thickness: $3.75{\cdot}10^{-5}$ m

4.3. Numerical Uncertainty

In CFD and experimental research, it is vital to comprehend the sources of uncertainty to validate the reliability of the results. Uncertainty in numerical simulations can arise from grid resolution and temporal discretization errors, while experimental uncertainty may result from measurement errors, instrument precision, and environmental conditions. A thorough analysis of these uncertainties allows for the assessment of result confidence levels and ensures robust and reliable conclusions.

The numerical uncertainty quantification was conducted using two different methods. Generally, it is recommended to use the American Society of Mechanical Engineers (ASME) 20-2009 standard for verification and validation (V&V) in computational fluid mechanics and heat transfer [24], which provides step-by-step an approach to verify and validate CFD models. The uncertainty quantification presented in the ASME 20-2009 standard for V&V relies on the grid convergence index (GCI) proposed by Roache [25]. One drawback of employing the GCI method is that its uncertainty solution is unreasonably small when the estimated order of accuracy (p_{RE}) is greater than the theoretical order of accuracy of the numerical method (p_{th}) [26]. Additionally, there is a lack of statistical information regarding the confidence level the GCI can achieve. The factor of safety (FS) method was considered in this study as well since this method provides a lower confidence limit of ≥ 1.2 at the 95% confidence level [26]. The following subsections overview the methodology followed to evaluate the convergence and uncertainty of CFD models.

4.3.1. Convergence study

An essential aspect of CFD modeling is to achieve numerical convergence, which can be evaluated. Before comparing different CFD modeling setups, it is crucial to establish a solid basis for evaluating the various physics model options. The numerical convergence of the CFD models discussed in this study is evaluated using a systematic refinement of three grid sizes. The coarse (x_3), medium (x_2), and fine (x_1) meshes are refined based on a refinement ratio (r) of 1.4, as shown in Equation 19.

$$r = \frac{x_2}{x_1} = \frac{x_3}{x_2} \tag{19}$$

This approach systematically refines the computational grid by reducing the cell size by a factor of 1.4 while keeping the prism layers the same size and distribution throughout the model. This allows for more precise capture of flow features with smaller mesh sizes and better quantification of the results' dependence on grid resolution. Table 7 summarizes the mesh sizes and the corresponding number of cells resulting from the discretization of the geometry using this mesh refinement approach.

Table 7: Mesh sizes and corresponding number of cells used in the grid independence study.

	Mesh size (mm)	**Volume (m^3)**	**Number of Cells**			**x**
			Solid Region	**Fluid Region**	**Overall**	
Fine	0.2500	$5.7998 \cdot 10^{-4}$	11,839,681	15,867,955	27,707,636	$2.7560 \cdot 10^{-4}$
Medium	0.3750	$5.8028 \cdot 10^{-4}$	5,649,043	8,219,182	13,868,225	$3.4717 \cdot 10^{-4}$
Coarse	0.5625	$5.8062 \cdot 10^{-4}$	4,120,115	5,997,668	10,117,783	$3.8572 \cdot 10^{-4}$

For nonstructured grids, the representative mesh size can be obtained using the following equation [27]:

$$x = \left[\left(\sum_{i=1}^{N} \Delta V_i \right) / N \right]^{1/3}, \tag{20}$$

where N and ΔV_i are the total number of cells and the volume of the ith cell, respectively. The convergence ratio (R) is a metric used to evaluate the convergence behavior of a variable based on the value of R as the grid is refined [28]. The different convergence behaviors are listed below:

(a) Monotonic convergence: $0 < R < 1$
(b) Oscillatory convergence: $R < 0$ and $|R| < 1$
(c) Monotonic divergence: $R > 1$
(d) Oscillatory divergence: $R < 0$ and $|R| > 1$

The convergence ratio requires minimum three solutions for convergence evaluation, and it is calculated using the following set of equations:

$$R = \frac{\epsilon_{21}}{\epsilon_{32}} \tag{21}$$

$$\epsilon_{21} = S_2 - S_1 \tag{22}$$

$$\epsilon_{32} = S_3 - S_2 \tag{23}$$

From above, S_1, S_2, and S_3 are the solutions to the fine, medium, and coarse meshes, respectively. It is recommended that the solution's convergence behavior be evaluated prior to proceeding.

The Richardson extrapolation method is used to estimate the order of accuracy (p_{RE}) and error estimate (δ_{RE}), which are essential to calculate the distance from the asymptotic range and numerical uncertainties. These two values are calculated as follows:

$$p_{RE} = \frac{\ln\left(\epsilon_{32}/\epsilon_{21}\right)}{\ln\left(r\right)} \tag{24}$$

$$\delta_{RE} = \frac{\epsilon_{21}}{r^{p_{th}} - 1} \tag{25}$$

If the solutions are in the asymptotic range, the estimate order of accuracy is equal to the theoretical order of accuracy ($p_{RE} = p_{th}$). However, many solutions do not fall within the asymptotic range, resulting in $p_{RE} \neq p_{th}$. The distance to the asymptotic range is calculated using Equation 26.

$$P = \frac{p_{RE}}{p_{th}} \tag{26}$$

The convergence study for different CFD setups is discussed in Section 4.5.

4.3.2. Numerical Uncertainty Quantification Method

Previously, it was mentioned that this study calculates the numerical uncertainty using two methods, GCI and FS. The GCI is only used as a reference in this study to compare it against the factor of safety. Ultimately, the factor of safety is the adopted methodology for uncertainty quantification as it overcomes the two main deficiencies of the GCI method [26]. The numerical uncertainty using GCI (U_{GCI}) is calculated using Equation 27.

$$U_{GCI} = FS \frac{|\epsilon_{21}|}{r^{P_{RE}} - 1} = FS\, |\delta_{RE}| \tag{27}$$

where FS is the variable factor of safety. According to [25], a $FS = 3$ should be used when two-grid solutions are available using p_{th}. If at least three grid solutions are available using p_{RE}, then $FS = 1.25$.

The other numerical uncertainty calculation method, factor of safety (U_{FS}), uses an equation that is conditional to the value of P, as illustrated in Equation 28.

$$U_{FS} = FS(P)\,|\delta_{RE}| = \begin{cases} [FS_1 P + FS_0(1-P)]\,|\delta_{RE}|\,, & \text{if } 0 < P \leq 1 \\ [FS_1 P + FS_2(P-1)]\,|\delta_{RE}|\,, & \text{if } P > 1. \end{cases} \tag{28}$$

The constants FS_0, FS_1, and FS_2 are obtained from a statistical analysis using samples based on numerical and analytical benchmarks. The result of this statistical analysis indicates that the recommended values for FS_0, FS_1, and FS_2 are 2.45, 1.6, and 14.8, respectively [26]. Therefore, Equation 28 can be written in the following form:

$$U_{FS} = FS(P)\,|\delta_{RE}| = \begin{cases} (2.45 - 0.85P)\,|\delta_{RE}|\,, & \text{if } 0 < P \leq 1 \\ (16.4P - 14.8)\,|\delta_{RE}|\,, & \text{if } P > 1. \end{cases} \tag{29}$$

4.4. Initial and Boundary Conditions

In the CFD models developed for this study, boundary conditions were meticulously defined to mirror the experimental setup, where the TPMS structure was electrically heated. Heat generation within the TPMS was simulated by imposing a volume heating boundary condition, with the power adjusted to match the power input applied in the experiments. At the inlet, a mass flow rate boundary condition was applied based on the experimentally measured mass flow rate, ensuring that the airflow entering the domain accurately reflected the experimental conditions. Additionally, the inlet air temperature was set according to the experimentally recorded values to maintain thermal consistency. The outlet was modeled with a pressure-outlet condition, simulating atmospheric conditions by setting the gauge pressure to near ambient levels. This comprehensive approach ensured that the CFD simulations closely replicated the experimental environment, providing reliable and comparable results.

Regarding initial conditions, the simulations were initialized with a uniform air temperature and static pressure throughout the computational domain, closely aligning with the initial conditions of the experimental setup. The initial velocity field was set to zero, representing a flow starting from rest and allowing the flow to develop naturally as the simulation progressed. The initial temperature of the TPMS was set according to the pre-heating conditions documented in the experiments. The electrical heating of the TPMS was applied instantaneously to minimize computational costs associated with simulating the heating process. For each experimental setting, the previous flow conditions were used as new initial conditions to ensure continuity and further reduce computational costs by avoiding the need to start each simulation from a zero velocity field and calculate the entire flow development from scratch. By ensuring that both the boundary and initial conditions, including the heat input from the electrically heated TPMS, were consistent with the experimental setup, the CFD models provided a reliable basis for comparing temperature and flow behavior. This rigorous approach ensured that the simulations accurately reflected the dynamics observed experimentally, thereby validating the computational results.

4.5. Physics Models

The selection process for the physics models of the solid region was a straightforward process. The electrically conductive material used to 3D print the TPMS was assumed to have a constant density, thermal conductivity, and specific heat capacity of 1240 kg/m^3, 0.13 W/m/K, and 1210 J/kg/K, respectively. Since the TPMS was electrically heated, the solid energy model was activated.

The selection process for physics models in the fluid region requires careful consideration. The TPMS experiments utilized air as the HTF, with its thermophysical properties at atmospheric pressure described by the polynomial functions summarized in Table 8. Modeling the fluid dynamics within a TPMS structure can be approached using various physics settings, each with its own advantages and disadvantages depending on the specific case. Consequently, a comparative study is presented below, evaluating different settings and highlighting their respective pros and cons.

Table 8: Thermo-physical properties of air at atmospheric pressure, with polynomial expressions valid over the temperature range of 250 to 950 K [29, 30].

Property	Function
Density [kg/m^3]	$\rho = 8.2398 \cdot 10^{-12}T^4 - 2.4234 \cdot 10^{-8}T^3 + 2.7246 \cdot 10^{-5}T^2 - 1.4551 \cdot 10^{-2}T + 3.6701$
Thermal conductivity [W/m/K]	$k = -8.3709 \cdot 10^{-9}T^2 + 7.9348 \cdot 10^{-5}T + 3.1921 \cdot 10^{-3}$
Specific heat capacity [J/kg/K]	$Cp = -3.1234 \cdot 10^{-7}T^3 + 7.3833 \cdot 10^{-4}T^2 - 3.3198 \cdot 10^{-1}T + 1048.95$
Viscosity [Pa-s]	$\mu = 1.4467 \cdot 10^{-14}T^3 - 4.2602 \cdot 10^{-11}T^2 + 6.8382 \cdot 10^{-8}T + 1.3689 \cdot 10^{-6}$

4.5.1. K-omega (Menter) SST vs. realizable k-epsilon: steady temporal solver

STAR-CCM+ offers several turbulence models, with the realizable k-ε two-layer and k-ω (Menter) SST being two commonly used options. The realizable k-ε two-layer turbulence model, which is a two-transport-equation model that solves for the kinetic energy (k) and turbulent dissipation (ε), was chosen for evaluation due to its robustness, relatively simple formulation and improved prediction of turbulent flows compared to the standard k-ε model. Realizable k-ε has been used in other studies that evaluate the thermal-hydraulic performance of TPMS structures [5, 31]. Consequently, the realizable k-ε turbulence model was chosen for this evaluation study, while the standard k-ε model was excluded from consideration.

Similarly, the k-ω (Menter) SST model, which is also a two-transport-equation model solving for turbulent kinetic energy (k) and specific dissipation rate (ω), was evaluated for modeling fluid dynamics within a TPMS geometry. This model provides superior turbulence prediction compared to the standard k-ω model by using a blending function to combine the Wilcox k-ω model near walls with the standard k-ε model away from walls [32]. Therefore, the k-ω (Menter) SST model was included in this study.

The initial comparison aimed to assess the performance of these turbulence models using segregated flow under steady-state conditions. Despite identical initial and boundary conditions, the models differed in their turbulence model choice. Figure 8 visually compares the numerical results of the aforementioned k-ω and k-ε turbulence models with experimental data across three different mesh sizes, with the experimental measurement shown as a dashed line. The analysis indicates that the k-ω (Menter) SST model outperforms the realizable k-ε model, particularly in predicting pressure drop accuracy when using a segregated flow solver. Several potential reasons for these results include:

1. TPMS surfaces have inherently complex geometries that make it challenging to predict flow near the wall. The k-ω (Menter) SST model provides superior near-wall treatment compared to the realizable k-ε model, which could improve the accuracy of pressure drop predictions.
2. Flow separation and reattachment are crucial phenomena in TPMS structures, particularly as the flow may separate and reattach multiple times due to the periodic nature of the surface. The k-ω (Menter) SST model excels in predicting these phenomena, positively impacting pressure drop predictions.
3. The k-ω (Menter) SST model is better suited for flows involving complex curvature and intricate geometries, which are characteristic of TPMS. This model can handle the effects of adverse pressure gradients and flow separation more effectively than the realizable k-ε model.

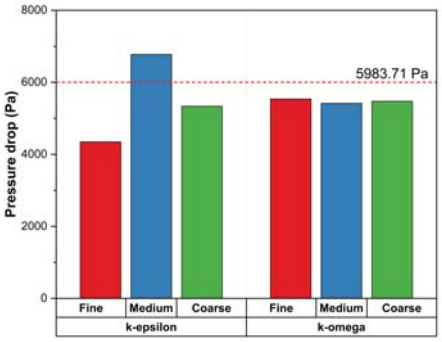

(a) Pressure drop across TPMS.

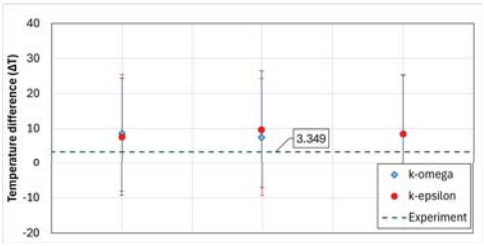

(b) TPMS outlet temperature.

Figure 8: Comparison of turbulence models: Bar plot illustrating the performance of the realizable k-epsilon and k-omega (Menter) SST models under steady-state conditions.

The comparison analysis also demonstrated that the realizable k-ε model produced results faster than the k-ω (Menter) SST model. However, it negatively impacted the accuracy of the

predicted pressure drop. Additionally, we consistently encountered a challenge when using these two turbulence models, as the convergence ratio (R) fell below -1.0, indicating oscillatory divergence in the results.

4.5.2. K-omega (Menter) SST: implicit unsteady temporal solver

Initially, the CFD models were executed using a steady-state solver, with results averaged over 500 iterations using statistical reporting. However, numerical instability and high residual values, particularly in the turbulence dissipation rate, were observed when using the k-ω (Menter) SST model. To achieve numerical stability and convergence, the temporal solver was switched from steady-state to implicit unsteady.

A comparison analysis was conducted to evaluate the numerical results, convergence, and stability of a TPMS CFD model using the k-ω (Menter) SST model, which showed slight superiority over the realizable k-ε model. The variable under consideration was the temporal solver, with both steady-state and implicit unsteady solvers tested.

For the steady-state solver CFD model, the residuals reached values below $1 \cdot 10^{-7}$ across most variables, except for the turbulence dissipation rate residuals, which remained relatively high. Additionally, as shown in Figure 9, despite the residuals leveling out, the numerical results exhibited instability. The temporal solver was then changed from steady-state to implicit unsteady with a time-step of $1 \cdot 10^{-6}$ seconds. After two time steps, the numerical results showed stability. As the simulation reached numerical stability, the residuals decreased significantly, reaching absolute values below $1 \cdot 10^{-4}$.

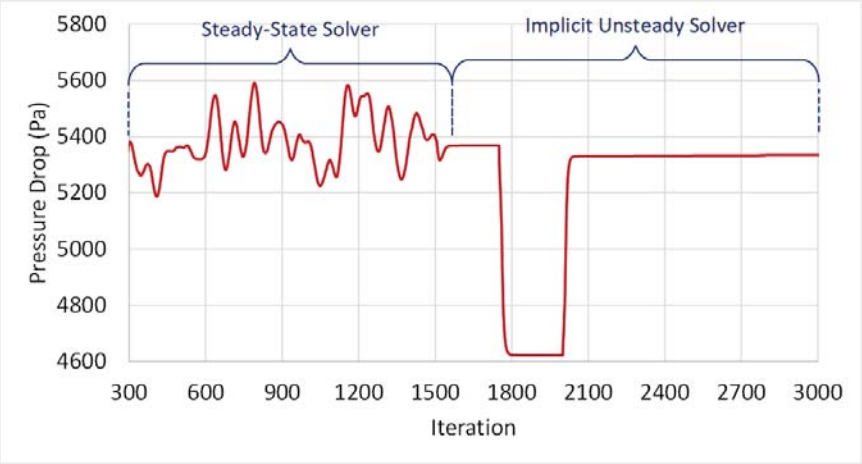

Figure 9: Comparison of pressure drop results using steady-state and implicit unsteady temporal solver with a k-ω (Menter) SST turbulence model, showcasing the impact of the temporal solver option on the numerical stability.

One challenge faced when evaluating the implicit unsteady CFD model is that the outlet temperature results indicated oscillatory divergence behavior (R=-3.5792), while the pressure drop results indicated oscillatory convergence (R=-0.7240). The comparison of steady-state and implicit unsteady temporal solvers is illustrated in Figure 10.

These results indicate that an implicit unsteady temporal solver could improve numerical stability and reduce turbulence dissipation rate residuals. Nonetheless, the computational cost

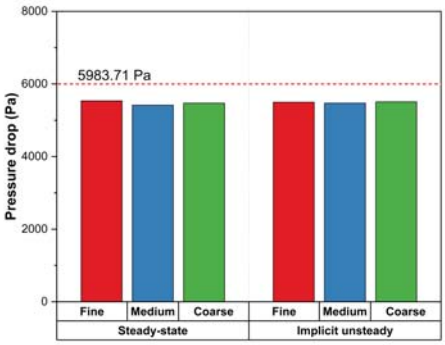

(a) Pressure drop across TPMS.

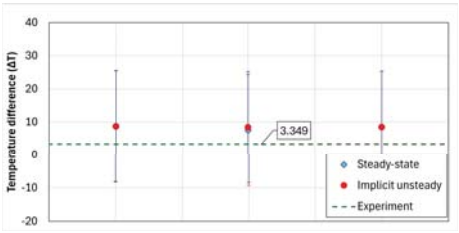

(b) TPMS outlet temperature.

Figure 10: Bar plot illustrating the performance of the k-omega (Menter) SST turbulence model using steady-state and implicit unsteady temporal solvers.

increased significantly when using an implicit unsteady CFD model. Despite the benefits of using an implicit unsteady time solver, the authors decided to explore alternative configurations to achieve solution convergence and numerical stability while using computationally efficient CFD models.

4.5.3. Constitutive Relationships

Most RANS turbulence models typically use the Boussinesq approximation for closure of the turbulence in the system of equations. This approximation assumes that the turbulent stress tensor is proportional to the mean shear stress tensor in the flow, thus introducing the concept of turbulent eddy viscosity. Therefore, RANS equations using this approximation are known as eddy viscosity models. Modifications to the Boussinesq approximation can be made in certain k-ω and k-ε turbulence models through the use of nonlinear constitutive relationships to improve accuracy [33].

Three options for the constitutive relationship of k-ω are available. The default choice is a linear relationship, but this study examines the other available constitutive relationship options for the k-ω (Menter) SST model: the quadratic constitutive relation (QCR) and cubic. Altering the constitutive relationship can potentially improve the turbulence model's performance when predicting turbulence in flows with strong secondary recirculation, streamline curvature, or under highly non-equilibrium conditions [34].

The first comparison evaluates the k-ω (Menter) SST model using a steady-state time solver with three different constitutive relationships. The comparison of the three different options is showcased in Figure 11. While the pressure drop and outlet temperature results differ by small amounts, the solution convergence varied from case to case. The convergence ratio of each case scenario is summarized in Table 9.

The results presented in Table 9 indicate that a linear relationship does not yield convergent results for both pressure drop and outlet temperature. A QCR relationship improves solution convergence, resulting in oscillatory convergence for pressure drop and monotonic convergence for outlet temperature. The cubic constitutive relationship yielded solutions that indicate monotonic convergence for both pressure drop and outlet temperature. These results highlight the importance of adjusting the constitutive relationship. The results provided above are from CFD models

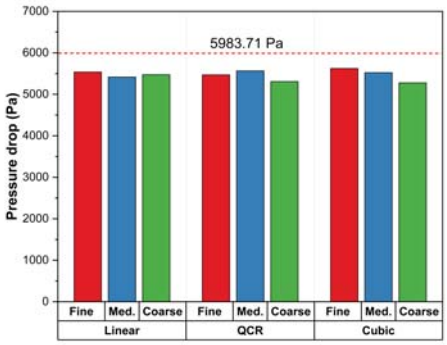

(a) Pressure drop across TPMS.

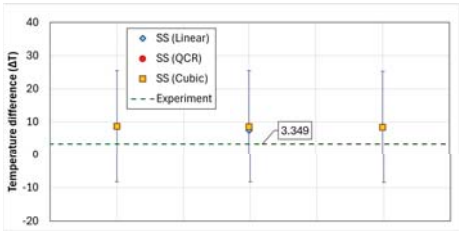

(b) TPMS outlet temperature.

Figure 11: Bar plot illustrating the performance of the k-ω (Menter) SST turbulence model under steady-state conditions with different constitutive relationships.

Table 9: Solution convergence for CFD models with different constitutive relationships.

Constitutive relationships	Option	Mesh			Convergence ratio (-)
		Fine	Medium	Coarse	
Linear	Pressure drop	5536.05	5415.70	5473.77	-2.0725
	Outlet temperature	301.6342	300.5003	301.5387	-1.0919
QCR	Pressure drop	5469.63	5564.66	5309.18	-0.3720
	Outlet temperature	301.6369	301.5992	301.4492	0.2517
Cubic	Pressure drop	5623.44	5522.24	5277.18	0.4130
	Outlet temperature	301.7015	301.5638	301.3903	0.7937

using a steady-state temporal solver. However, the authors wanted to investigate the impact of the constitutive relationships when implementing an implicit unsteady mode, which is discussed below.

The impact of the constitutive relationships on the numerical solutions is also evaluated using an implicit unsteady temporal solver. The results of this comparison analysis are presented in Figure 12. It is important to note that when testing the cubic option with a steady-state temporal solver, the CFD model reached numerical convergence and yielded reasonably good results when compared to experimental data. However, the results of the CFD model that used the implicit unsteady temporal solver could not be analyzed as the simulation became highly unstable. Therefore, the results of the CFD model that uses the cubic constitutive relationship could not be presented.

The use of a QCR constitutive relationship did not yield significant improvements in the numerical results compared to the model that used the linear constitutive relationship. However, the numerical solution convergence did improve, as the outlet temperature exhibited an oscillatory convergence behavior when a linear constitutive relationship was used. The numerical solution changed to monotonic convergence when using the QCR constitutive relationship. The main drawback of using an implicit unsteady time solver is the considerable increase in computational time compared to the steady-state CFD models.

To further enhance solution convergence, the *low Re damping modification* option was ac-

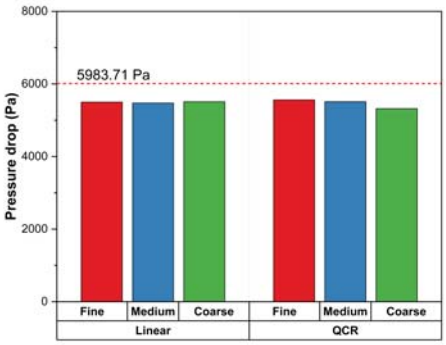

(a) Pressure drop across TPMS.

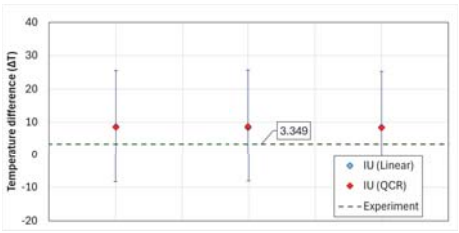

(b) TPMS outlet temperature.

Figure 12: Bar plot illustrating the performance of the k-omega (Menter) SST turbulence model using the implicit unsteady time solver with different constitutive relationships.

tivated. This option is often associated with the simulation of flows at low Reynolds numbers, where the flow is more laminar than turbulent. In such cases, damping oscillations or fluctuations in the flow becomes crucial to achieve a stable and accurate solution [34]. It is important to note, however, that caution should be exercised when running simulations with high Reynolds numbers, as the low Re damping modification may not be suitable and could potentially lead to inaccurate results.

A comparison of the CFD model with the low Re option activated versus deactivated is summarized in Table 10, demonstrating an improvement in numerical solution convergence. Specifically, the outlet temperature and pressure drop solutions exhibit monotonic convergence behavior with the low Re option activated.

Table 10: Solution convergence of steady-state CFD models with QCR constitutive relationship with and without Low Re damping modification.

Low Re Damping Modification	**Option**	**Mesh**			**Convergence ratio (-)**
		Fine	**Medium**	**Coarse**	
Activated	Pressure drop	5498.6781	5466.7719	5277.1763	0.1683
	Outlet temperature	301.6496	301.5886	301.3903	0.3075
Deactivated	Pressure drop	5469.63	5564.66	5309.18	-0.3720
	Outlet temperature	301.64	301.60	301.45	0.2517

4.5.4. k-omega (Menter) SST vs. LEB k-epsilon

So far, the comparison analysis has been addressed using realizable k-ε and k-ω (Menter) SST turbulence models with different options activated. Another model proposed in past studies to predict flow turbulence is the LEB model. One of the advantages of k-ε over k-ω is that the turbulence dissipation rate formulation is more stable [35]. The LEB k-ε turbulence model exhibits superiority over realizable k-ε in terms of accuracy in the near-wall region and better numerical stability than k-ω SST [35].

The LEB model is a turbulence model that solves the transport equations for turbulent kinetic energy (k), turbulent dissipation rate (ε), the normalized wall-normal stress component, and the

elliptic blending factor (α) to calculate the turbulent eddy viscosity. This model is particularly useful in CFD for simulating turbulent flows [35] as it combines the stress-strain lag concept introduced by [21]. The simulation using the LEB k-ε turbulence model was compared to the k-ω (Menter) SST with QCR constitutive relationship at low Re using a steady temporal solver. The results of this comparison for the steady time solver are depicted in Figures 13.

The results obtained from using LEB k-ε indicate that numerical stability was improved even when a steady-state temporal solver was used. The k-ω (Menter) SST model under steady-state conditions was better at predicting the pressure drop within the TPMS, with the maximum difference between numerical and experimental results being 11.8% using a coarse mesh. In contrast, when using the fine mesh, the LEB k-ε model predicted the pressure drop with a 23.9% difference. Regarding outlet temperature prediction, the LEB k-ε model performed better, with the maximum reported difference compared to experimental data being 4.74°C when using a coarse mesh. On the other hand, the k-ω (Menter) SST over-predicted the temperature by 5.26°C. The numerical solution convergence behavior for both CFD models was monotonic convergence.

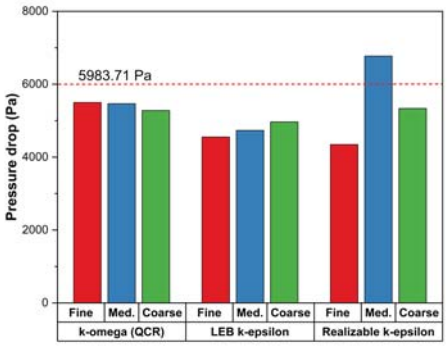

(a) Pressure drop across TPMS.

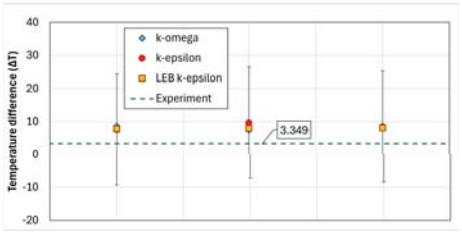

(b) TPMS outlet temperature.

Figure 13: Bar plot illustrating the performance of the k-ω (Menter) SST, LEB, and realizable k-ε turbulence models using the steady time solver.

4.5.5. Segregated vs. coupled flow solver

The performance of the k-ω (Menter) SST model was evaluated using both segregated and coupled flow solvers. The studies discussed earlier primarily relied on segregated solvers, which solve the governing flow equations sequentially, simplifying the computational process. However, the coupled flow solver, which simultaneously solves these equations, offers potential advantages, particularly in terms of capturing tighter coupling between variables and improving convergence behavior in complex flows. Despite these benefits, the use of coupled solvers comes with a significant drawback: the computational cost increases substantially. This is because coupled solvers take longer to reduce residuals and achieve convergence, requiring more iterations and higher memory usage compared to segregated solvers.

Given the considerable computational expense associated with the coupled solver, particularly in the context of the CFD models used in this study, the authors decided to forgo its implementation. Nonetheless, the authors encourage others to consider the coupled solver in future evaluations, as it may offer improved accuracy or stability in certain scenarios. This decision should be weighed against the potential increase in computational resources required.

The segregated flow solver was chosen and performed well. When combined with the steady-state temporal solver, it produced results that closely matched experimental data and consistently achieved numerical convergence across all parameters of interest. This shows that the segregated solver is reliable and computationally efficient for the flow conditions and turbulence models studied.

5. Experimental vs. Numerical Results

This section focuses on comparing the pressure drop, temperatures, and heat transfer coefficient of a gyroid TPMS geometry between experimental and numerical results. Assessing the hydraulic efficiency of heat exchangers heavily relies on pressure drop, as it directly influences the energy required to maintain fluid flow through the system. The complex geometry of the gyroid TPMS presents unique challenges for accurately predicting pressure drop using CFD simulations. Therefore, directly comparing experimentally measured pressure drops with those predicted by the CFD model provides valuable insights into the reliability and accuracy of the numerical simulations.

Accurate temperature measurements are crucial for determining the thermal performance of the TPMS geometry. Comparing experimental temperature data with CFD predictions helps validate the model's capability to capture the thermal behavior of the system. The embedded thermocouples used in the experiments enable precise temperature measurements at various points within the lattice, allowing for a detailed comparison between experimental and numerical results. Furthermore, the heat transfer coefficient is a key parameter for evaluating the convective heat transfer performance of the gyroid TPMS. By comparing the heat transfer coefficients derived from experimental data with those obtained from CFD simulations, we can assess the model's accuracy in predicting convective heat transfer.

For the benchmark analysis, the k-ω (Menter) SST model with QCR and Low Re options was selected, utilizing a steady-state solver. Before comparing experimental and numerical data, it is crucial to quantify numerical uncertainty. This was meticulously analyzed through a grid independence study, employing a refinement ratio of 1.4, which provides a robust basis for evaluating the impact of grid resolution on simulation outcomes. Both the GCI and FS methods were implemented to estimate the numerical uncertainties and identify the most appropriate method for further uncertainty quantification. As shown in Table 11, the convergence ratio, order of accuracy, distance to the asymptotic range, error estimate, and uncertainties from both methods are presented. The table highlights that the FS method provides more conservative values compared to the GCI method. Additionally, it showcases the convergence ratios for critical parameters such as pressure drop and outlet temperature, indicating monotonic convergence. For conservative purposes, the uncertainty obtained through the FS method is employed in subsequent analyses. This integrated approach ensures a more accurate comparison between numerical predictions and experimental data, ultimately leading to more robust conclusions regarding the performance of the CFD model.

The pressure drop across the gyroid TPMS is the first parameter compared between numerical and experimental data. Experimentally collected measurements are plotted alongside numerical results obtained from simulations, where the TPMS power generated remained relatively constant at approximately 78.4 W. In our analysis, we conducted a comprehensive comparison, evaluating model performance at both low and high flow rates. This approach allowed us to assess the numerical stability of the model under different flow conditions. The comparison results between experimental and numerical data are visually represented in Figure 14, providing

Table 11: Numerical uncertainty quantification of CFD model, using k-ω (Menter) SST with QCR and LowRe options activated.

Parameter	Convergence ratio R (-)	P_{Re}	P	δ_{Re}	U_{FS}	U_{GCI}
Pressure drop	0.1683	5.30	2.6506	6.4558	185.08	8.07
Outlet temperature	0.5109	2.00	0.9990	0.1095	0.18	0.14

insights into the performance and reliability of the models under varying flow conditions. This visual representation facilitates a clear understanding of the models' accuracy and highlights any discrepancies between the experimental and numerical results.

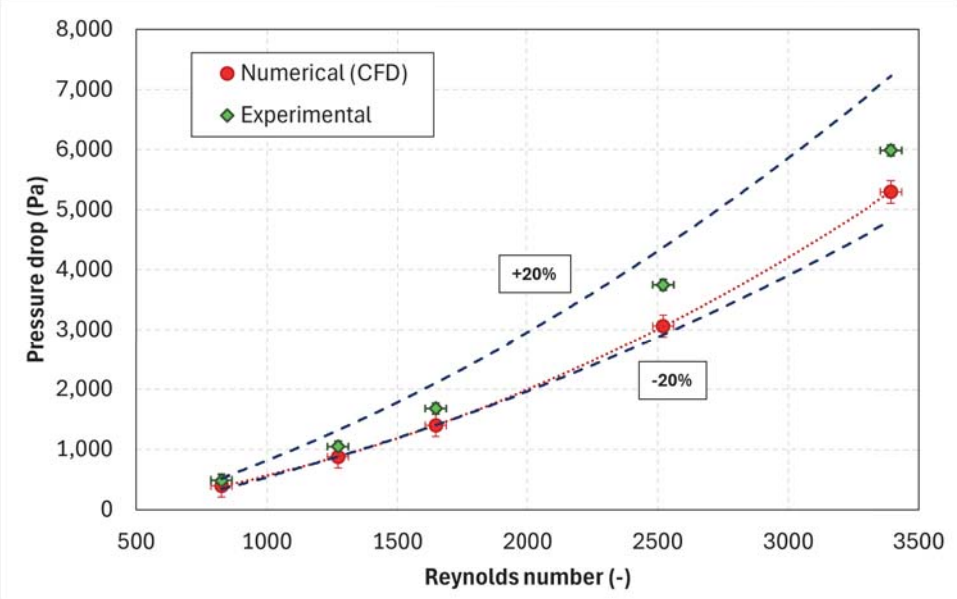

Figure 14: Comparison between experimental and numerical pressure drop results with a constant power input of a gyroid TPMS.

Initial findings from the benchmark analysis reveal that while the CFD model captured the overall trend of pressure drop across the gyroid structure, discrepancies were observed between the experimental and numerical results as the flow rate transitioned from laminar to turbulent. This variance could be attributed to the complexities of accurately resolving turbulence and flow separation within the highly convoluted TPMS geometry. Although the CFD model exhibited numerical stability at low flow rates, numerical instability increased as the flow rate rose. Additionally, the analysis of the constitutive relationships indicates that the *Low Re* option is adequate for handling low Reynolds numbers but may not be suitable for high Reynolds number values, which could be a factor impacting the numerical results. To further investigate any potential bias, a one-to-one comparison of pressure drop measurements obtained experimentally and numerically is presented in Figure 15.

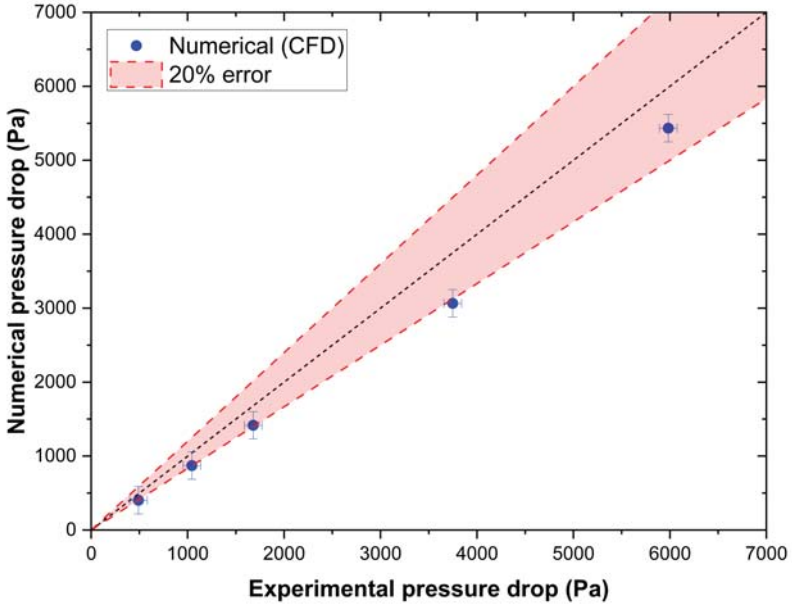

Figure 15: One-to-one pressure drop comparison between experimental and numerical data collected with 20% error margin shaded.

Figure 15 indicates that the CFD model underpredicts the pressure drop by about a consistent 20% or less for varying flow rates. Despite this drawback, the k-ω (Menter) SST model outperformed previously mentioned CFD models with different turbulence models and settings.

The temperature difference between the inlet and outlet of the HTF was another parameter evaluated against experimental data. As air flows through the gyroid TPMS geometry, convective heat transfer removes heat, causing the temperature of the air to rise. This parameter is crucial as it provides insights into the heat transfer characteristics of the gyroid TPMS and aids in characterizing the heat transfer coefficient. The gyroid TPMS was subjected to various power inputs (38.08, 61.92, 79.20, and 124.55 W) at a constant flow rate of approximately 0.005 kg/s. The results of this comparative analysis are illustrated in Figure 16.

igure 16 illustrates that the CFD model generally overestimates the temperature difference. Nonetheless, most of the predicted temperature differences fall within the error margins of the experimental measurements. This indicates that while the model tends to predict slightly higher temperatures—particularly at the outlet—it maintains an acceptable range of accuracy.

To identify any potential bias, a one-to-one comparison of the temperature difference between the inlet and outlet for the HTF using both experimental and numerical data is conducted. This comparison, presented in Figure 17, facilitates a direct evaluation of the model's performance against actual measurements. By analyzing this comparison, researchers can better understand the discrepancies between the model and experimental data. This analysis can inform further refinements of the CFD model or adjustments in experimental procedures, thereby improving the alignment between the two. This iterative process is essential for enhancing the accuracy and reliability of the CFD simulations in predicting the thermal performance of the gyroid TPMS.

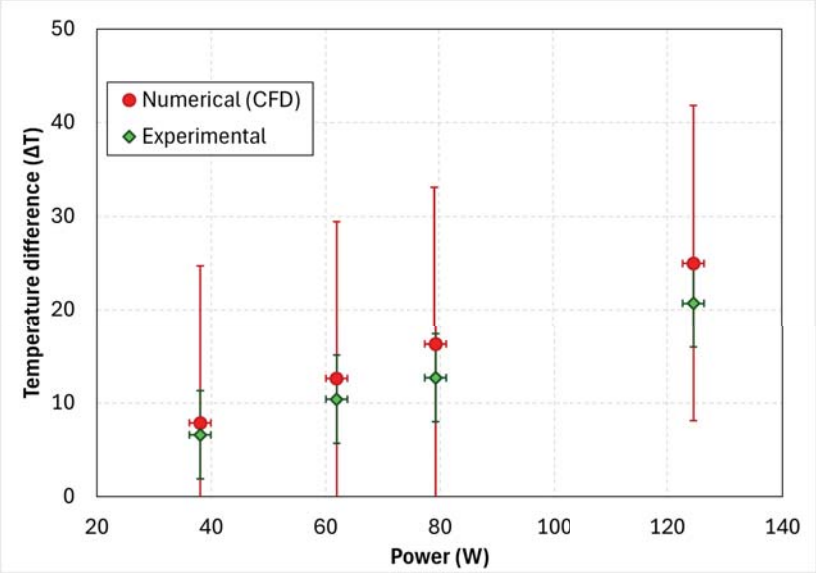

Figure 16: Comparison between experimental and numerical HTF temperature difference results of an electrically heated gyroid TPMS.

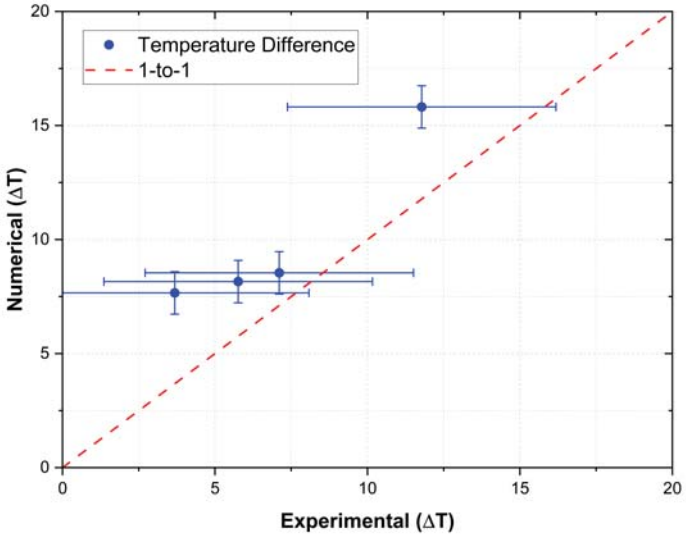

Figure 17: One-to-one comparison of inlet and outlet temperature differences for HTF using experimental and numerical data.

Figure 17 suggests that the measurements may under-report the temperature difference between the inlet and outlet. According to the uncertainty quantification of these measurements,

most of the uncertainty is attributed to the accuracy of the thermocouples (TCs). While the discrepancy between the experimental and numerical data can largely be attributed to the underestimation by the temperature measurements, it is also partly influenced by the overestimation from the CFD model. Despite these differences, the CFD results remain within an acceptable range of accuracy.

The temperature distribution within the TPMS was measured in the solid region to compare the experimental and CFD results. In Figure 18, the experimental measurements in the solid region reveal a broader temperature distribution from the inlet to the outlet sections of the TPMS. The high temperature measurements observed in the solid region near the outlet, except for the 38.08W power experiment, but lower temperatures in the middle and inlet sections, can be attributed to several factors: (1) the reduced thermal mass and increased porosity of the lattice may cause localized hotspots, particularly near the outlet where the fluid has already absorbed heat. This can result in higher temperatures in the solid region close to the outlet compared to other sections; (2) the infill combined with the sensor placement could have impacted the measurements as the increase of power in the lattice had little effect in the inlet and mid-point temperature measurements. In contrast, the CFD simulations show a more uniform and narrower temperature distribution along the same path. The narrower temperature gradient in the solid structure within the CFD model leads to less heat being transferred to the fluid, impacting the accuracy of temperature predictions, particularly near the inlet where the largest heat transfer gradients are expected.

Furthermore, it is important to note that the 3D-printed lattice has an infill percentage of less than 100%. This reduced infill means the lattice contains less material, resulting in a diminished thermal mass. Consequently, the lattice heats up more rapidly, potentially causing higher fluid temperatures at the inlet and reducing the temperature difference between the inlet and outlet. This could explain why the experimental data shows lower temperature differences compared to the CFD data.

The temperature distribution within the TPMS was measured in the solid region to compare the experimental and CFD results. In Figure 18, the experimental measurements in the solid region reveal a broader temperature distribution from the inlet to the outlet sections of the TPMS. Notably, higher temperature measurements were observed in the solid region near the outlet when compared to the numerical data, except for the 38.08 W power experiment, while lower temperatures were recorded in the middle and inlet sections. This discrepancy can be attributed to several factors:

1. The reduced thermal mass and increased porosity of the lattice may cause localized hotspots, particularly near the outlet where the fluid has already absorbed heat. This can result in higher temperatures in the solid region close to the outlet compared to other sections.
2. The combination of reduced infill and sensor placement could have impacted the measurements. This could explain why the increase in power within the lattice had little effect on the solid inlet and mid-point temperature measurements.

In contrast, the CFD simulations show a more uniform and narrower temperature distribution along the same path. The narrower temperature gradient in the solid structure within the CFD model results in less heat being transferred to the fluid, affecting the accuracy of temperature predictions, particularly near the inlet where the largest heat transfer gradients are expected.

The performance of TPMS nuclear fuel lattices is critically dependent on efficient convective heat transfer, making the heat transfer coefficient (h) a crucial parameter to accurately character-

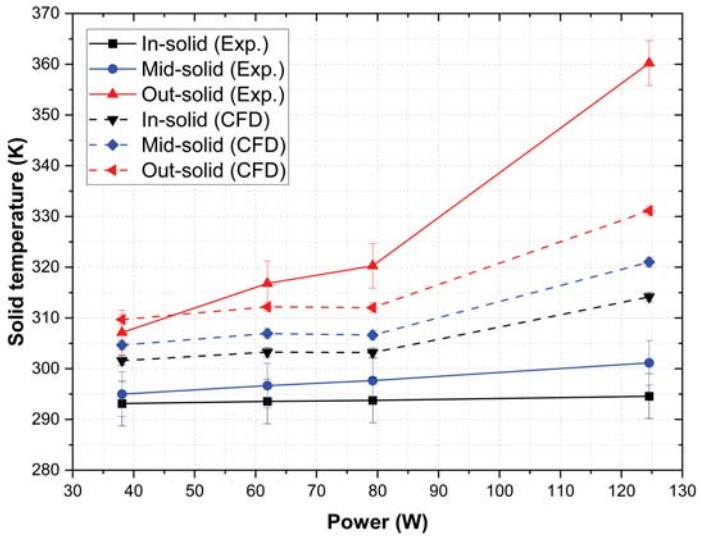

Figure 18: Comparison of temperature measurements at the inlet, middle, and outlet sections of the solid region of the gyroid TPMS. Experimental data are represented by solid lines, while numerical data are depicted with dashed lines.

ize. Initial efforts were made to predict the heat transfer coefficient using temperature measurements obtained from embedded thermocouples (refer to Figure 3). Accurate characterization of (h) is essential for optimizing the thermal performance and safety of TPMS nuclear fuel lattices.

The convective heat transfer coefficient is defined as follows [36]:

$$h = \frac{\dot{Q}}{A_s(T_{wall} - T_{fluid})} \tag{30}$$

The power ($\dot{Q}$) is obtained from the power applied to the lattice through the power supply. The heat transfer surface area (A_s) is derived from the STL model used to 3D print the lattice. The fluid temperature (T_{fluid}) and wall temperature (T_{wall}) are measured using the embedded thermocouples shown in Figure 3. While the heat transfer coefficient can be determined from these experimental measurements, its accuracy depends heavily on the precision of the variables involved. One significant challenge in this approach is the accurate measurement of the wall temperature [37].

Measuring wall temperature is particularly challenging due to several factors that can compromise accuracy. One critical factor is the thermal resistance caused by the thermal contact between the temperature sensor and the wall. This thermal contact resistance can lead to discrepancies between the actual wall temperature and the measured temperature. Additionally, thermal lag due to the sensor's response time, heat conduction along the thermocouple wires, and potential signal interference from electrical noise can further affect the accuracy of the measurements. Variations in the material properties at the sensor location, such as differences in thermal conductivity or surface roughness, can also influence the readings. Moreover, the placement and embedding process may introduce mechanical stress and strain, potentially altering the sensor's performance.

A comparison of heat transfer coefficients, derived from experimental data and numerical CFD simulations, was conducted. The heat transfer coefficients from the inlet, middle, and exit sections of the lattice were calculated and averaged. The results, illustrated in Figure 19, demonstrate that the predicted values from the CFD model and the experimentally calculated values generally fall within the error margins. However, a closer examination reveals distinct trends based on the flow regime. In the laminar flow region, the CFD model tends to underpredict the heat transfer coefficient, whereas for flow in the turbulent regime, the model overpredicts the heat transfer coefficient.

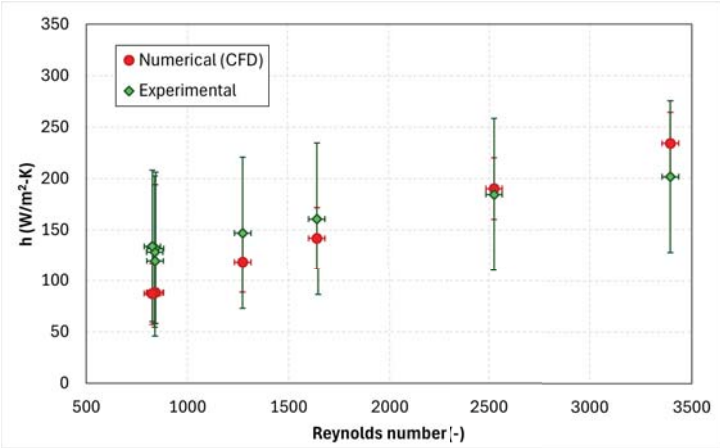

Figure 19: Comparison of heat transfer coefficients calculated from experimental data using embedded thermocouples and predicted by numerical CFD simulations.

The maximum difference between the numerical results and those calculated from experimental data is 46.78 W/m^2-K, with the smallest difference being 5.70 W/m^2-K. These results highlight the critical importance of implementing correction factors for wall temperature measurements to enhance the accuracy of the heat transfer coefficient. By refining our measurement techniques and incorporating these correction factors, we can significantly improve the reliability of our heat transfer calculations. These initial studies provide valuable insights that will inform future research efforts, enabling us to develop more precise and accurate methodologies for determining heat transfer coefficients. This, in turn, will lead to a better understanding and optimization of TPMS nuclear fuel lattice designs.

6. Conclusion

The adoption of complex geometries, such as TPMS, has gained substantial traction across various industries, particularly in the nuclear and thermal management sectors, due to their exceptional thermal-hydraulic properties and potential for enhancing heat transfer efficiency. TPMS structures, such as the gyroid and diamond, have demonstrated considerable promise in improving heat exchange processes, making them viable alternatives to traditional designs. Despite the growing interest, there remains a significant gap in the literature concerning comprehensive numerical analyses and standardized practices for effectively modeling these geometries using CFD tools.

This study provides a comprehensive analysis of TPMS lattices, including the validation of CFD models, evaluation of turbulence models, and detailed numerical uncertainty analysis. The key contributions of this work include establishing best practices for CFD modeling, conducting a benchmark analysis, and performing in-depth uncertainty and convergence studies. These findings advance the understanding and modeling of TPMS lattices and support the development of methodologies for future applications in the nuclear sector and beyond.

To address the gap in the existing literature, this study benchmarks the thermal-hydraulic performance of a gyroid TPMS geometry, focusing on key performance metrics such as pressure drop, fluid inlet/outlet temperature difference, and heat transfer coefficient. The results underscore the necessity of employing robust CFD methodologies to obtain accurate predictions. Specifically, the study demonstrates the value of using a steady-state temporal solver paired with the k-ω (Menter) SST turbulence model, with QCR and low Reynolds options activated, to enhance numerical stability and precision. However, caution is recommended when implementing the Low Reynolds option, as it could negatively impact numerical results when the flow falls within the turbulent regime.

Through the development of these best practices, this research lays a foundation for future studies and the broader industrial implementation of TPMS geometries. The enhanced understanding of their thermal-hydraulic behavior will support their adoption in sectors where optimized heat transfer and pressure drop characteristics are critical, such as nuclear technology. The insights gained from this study will ultimately drive innovation in advanced thermal management solutions, enabling more efficient and effective heat transfer systems. Moreover, the methodologies and findings presented here can serve as a reference for researchers and engineers, facilitating the development of next-generation TPMS-based applications that leverage their unique properties for improved performance.

By addressing the gaps in the current literature and providing a robust framework for CFD modeling and analysis of TPMS structures, this study significantly contributes to the advancement of thermal-hydraulic engineering. The integration of detailed geometric information, uncertainty quantification, and convergence studies ensures that the results are both reliable and applicable to real-world scenarios. As a result, this work not only enhances the scientific understanding of TPMS lattices but also paves the way for their practical implementation in various high-performance thermal systems. Future efforts will focus on further refining the CFD model and expanding experimental testing to include other fluids relevant to nuclear systems, ultimately driving the development of advanced TPMS applications.

References

[1] J. Shi, L. Zhu, L. Li, Z. Li, J. Yang, X. Wang, A tpms-based method for modeling porous scaffolds for bionic bone tissue engineering, Scientific reports 8 (2018) 7395.

[2] N. Martin, S. Seo, S. Balderrama Prieto, C. Jesse, N. Woolstenhulme, Reactor physics characterization of triply periodic minimal surface-based nuclear fuel lattices, Progress in Nuclear Energy 165 (2023) 104895. URL: https://www.sciencedirect.com/science/article/pii/S014919702300330X. doi:https://doi.org/10.1016/j.pnucene.2023.104895.

[3] B. Prussack, I. Jentz, T. A. Moreira, N. Woolstenhulme, C. Jesse, G. Nellis, M. Anderson, Thermal and hydraulic performance of volumetrically heated triply periodic minimal surface heaters, Applied Thermal Engineering 248 (2024) 123291. URL: https://www.sciencedirect.com/science/article/pii/S1359431124009591. doi:https://doi.org/10.1016/j.applthermaleng.2024.123291.

[4] P. Bean, R. A. Lopez-Anido, S. Vel, Numerical modeling and experimental investigation of effective elastic properties of the 3d printed gyroid infill, Applied Sciences 12 (2022). URL: https://www.mdpi.com/2076-3417/12/4/2180. doi:10.3390/app12042180.

[5] N. Baobaid, M. I. Ali, K. A. Khan, R. K. A. Al-Rub, Fluid flow and heat transfer of porous tpms architected heat sinks in free convection environment, Case Studies in Thermal Engineering 33 (2022) 101944.
[6] M. Vlahinos, R. O'Hara, Unlocking advanced heat exchanger design and simulation with ntop platform and ansys cfx, nTopology Inc (2020).
[7] L. K. Dharmalingam, V. Aute, J. Ling, Review of triply periodic minimal surface (tpms) based heat exchanger designs, in: International Refrigeration and Air Conditioning Conference, 2022, pp. 1–10.
[8] J. Iyer, T. Moore, D. Nguyen, P. Roy, J. Stolaroff, Heat transfer and pressure drop characteristics of heat exchangers based on triply periodic minimal and periodic nodal surfaces, Applied Thermal Engineering 209 (2022) 118192.
[9] B. W. Reynolds, C. J. Fee, K. R. Morison, D. J. Holland, Characterisation of heat transfer within 3d printed tpms heat exchangers, International Journal of Heat and Mass Transfer 212 (2023) 124264.
[10] Y. Fu, J. Bao, C. Wang, R. K. Singh, Z. Xu, G. Panagakos, CFD Study of Countercurrent Flow in Triply Periodic Minimal Surfaces with CO2BOL Solvent, Technical Report, Pacific Northwest National Lab.(PNNL), Richland, WA (United States), 2019.
[11] M. Hawken, S. Reid, D. Clarke, M. Watson, C. Fee, D. Holland, Characterization of pressure drop through schwarz-diamond triply periodic minimal surface porous media, Chemical Engineering Science 280 (2023) 119039. URL: https://www.sciencedirect.com/science/article/pii/S000925092300595X. doi:https://doi.org/10.1016/j.ces.2023.119039.
[12] Z.-y. Zhang, H. Zhang, J. Zhang, S.-k. Qin, M.-d. Duan, Study on flow field characteristics of TPMS porous materials, Journal of the Brazilian Society of Mechanical Sciences and Engineering 45 (2023) 188.
[13] Protoplant, Material data table, 2024. https://proto-pasta.com/pages/material-data-table.
[14] Rosemount-3051S, Rosemount 3051S Series of Instrumentation, Emerson, 2022. https://www.emerson.com/documents/automation/product-data-sheet-rosemount-3051s-series-of-instrumentation-en-73154.pdf.
[15] Rosemount-3051, Rosemount 3051 Pressure Transmitter, Emerson, 2023. https://www.emerson.com/documents/automation/product-data-sheet-rosemount-3051-pressure-transmitter-en-73134.pdf.
[16] Omega, Thermocouple types, https://www.omega.com/en-us/resources/thermocouple-types, 2024. Accessed: 2024-09-05.
[17] S. S. Hutagalung, Estimation optimal value of discharge coefficient in a venturi tubes, in: Journal of Physics: Conference Series, volume 1230, IOP Publishing, 2019, p. 012087.
[18] S. J. Kline, Describing uncertainties in single-sample experiments, Mech. Eng. 75 (1963) 3–8.
[19] B. E. Launder, D. B. Spalding, The numerical computation of turbulent flows, in: Numerical prediction of flow, heat transfer, turbulence and combustion, Elsevier, 1983, pp. 96–116.
[20] F. R. Menter, Two-equation eddy-viscosity turbulence models for engineering applications, AIAA journal 32 (1994) 1598–1605.
[21] A. Revell, S. Benhamadouche, T. Craft, D. Laurence, A stress–strain lag eddy viscosity model for unsteady mean flow, International Journal of Heat and Fluid Flow 27 (2006) 821–830. URL: https://www.sciencedirect.com/science/article/pii/S0142727X06000774. doi:https://doi.org/10.1016/j.ijheatfluidflow.2006.03.027, special issue of the 6th International Symposium on Engineering Turbulence Modelling and Measurements – ETMM6.
[22] S. D. I. Software, Simcenter STAR-CCM+ User Guide, version 2402, in: Theory, Siemens, 2024. URL: https://docs.sw.siemens.com/en-US/doc/226870983/PL20231122669335741.starccmp_userguide_html?audience=external.
[23] Siemens Digital Industries Software, Simcenter STAR-CCM+ User Guide, version 2402, in: Tips to troubleshoot a non-finite residual (Sdr) floating point error when using the SST K-Omega turbulence model, Siemens, 2021, p. 1. URL: https://support.sw.siemens.com/en-US/product/226870983/knowledge-base/KB000047115_EN_US.
[24] M. McHale, J. Friedman, J. Karian, Standard for verification and validation in computational fluid dynamics and heat transfer, The American Society of Mechanical Engineers, ASME V&V 20 (2009) 100.
[25] P. J. Roache, Verification and validation in computational science and engineering, volume 895, Hermosa Albuquerque, NM, 1998.
[26] T. Xing, F. Stern, Factors of safety for richardson extrapolation, Journal of Fluids Engineering 132 (2010) 061403. URL: https://doi.org/10.1115/1.4001771. doi:10.1115/1.4001771.
[27] C. J. Freitas, Standards and methods for verification, validation, and uncertainty assessments in modeling and simulation, Journal of Verification, Validation and Uncertainty Quantification 5 (2020) 021001.
[28] H. W. Coleman, F. Stern, A. Di Mascio and, E. Campana, The problem with oscillatory behavior in grid convergence studies, J. Fluids Eng. 123 (2001) 438–439.
[29] I. Dincer, Heat transfer in food cooling applications, CRC Press, 1997.
[30] C. Borgnakke, R. E. Sonntag, Thermodynamic and transport properties, Wiley, 1997.
[31] M. Alteneiji, M. I. H. Ali, K. A. Khan, R. K. A. Al-Rub, Heat transfer effectiveness characteristics maps for additively manufactured TPMS compact heat exchangers, Energy Storage and Saving 1 (2022) 153–161.
[32] F. Menter, Zonal two equation kw turbulence models for aerodynamic flows, in: 23rd fluid dynamics, plasmady-

namics, and lasers conference, 1993, p. 2906.
[33] S. D. I. Software, RANS turbulence using non-linear constitutive relationships including QCR, in: Support Center, Siemens, 2022, p. 1. URL: https://support.sw.siemens.com/en-US/product/226870983/knowledge-base/KB000032422_EN_US.
[34] S. D. I. Software, Simcenter STAR-CCM+ User Guide, version 2402, in: Controlling a K-Omega Model, Siemens, 2024, p. 1. URL: https://docs.sw.siemens.com/documentation/external/PL20220717079233442/en-US/userManual/starccmp_userguide_html/index.html.
[35] Siemens Digital Industries Software, Simcenter STAR-CCM+ User Guide, version 2402, in: Elliptic Blending Model, Siemens, 2024, p. 1. URL: https://docs.sw.siemens.com/documentation/external/PL20231122669335741/en-US/userManual/starccmp_userguide_html/STARCCMP/GUID-D41C365F-94BA-4086-B9F6-629F8A6427DD.html.
[36] L. C. Burmeister, Convective heat transfer, John Wiley & Sons, 1993.
[37] D. Martínez, F. Illán, J. Solano, A. Viedma, Embedded thermocouple wall temperature measurement technique for scraped surface heat exchangers, Applied Thermal Engineering 114 (2017) 793–801.